PCCP

PAPER

View Article Online
View Journal | View Issue

Cite this: *Phys. Chem. Chem. Phys.*, 2025, **27**, 16003

Inorganic chemistry, cluster formation and solvent stability of PIM-1/ZnO_xH_y hybrid membranes synthesized *via* vapor phase infiltration†

Benjamin C. Jean,[a] Yi Ren,[b] Ethan Read,[a] Dong-Chan Lee,[a] Faisal Alamgir,[a] Ryan P. Lively[b] and Mark D. Losego*[a]

Received 9th December 2024,
Accepted 1st July 2025

DOI: 10.1039/d4cp04645e

rsc.li/pccp

Vapor phase infiltration (VPI) is a vapor processing technique that converts polymers into organic–inorganic hybrid materials with modified properties. VPI of polymer membranes stabilizes against dissolution and swelling in organic liquids, opening up new opportunities for use in organic solvent reverse osmosis (OSRO) separations. However, the precise chemical structure of the infiltrated inorganic components remains poorly understood, limiting the potential to fully exploit process–structure–property relations for materials design and slowing the development of new hybrid membranes. This study explores the structural characteristics contributing to the chemical stability of PIM-1/ZnO_xH_y hybrid membranes through advanced spectroscopic techniques to clarify the chemistry and inorganic cluster formation in these materials that lead to enhanced stability in solvents that otherwise swell or dissolve the pure polymer. X-ray photoelectron spectroscopy (XPS) indicates a predominantly zinc hydroxide chemistry with higher proportions of oxide forming only at increasing cycle counts. Extended X-ray absorption fine structure (EXAFS) spectroscopy provides new understanding of the first and second coordination shells. These results indicate that the size of the clusters increases with prolonged VPI precursor exposure and additional VPI cycles, leading to improvements in membrane solvent stability. These findings offer a new understanding for how the physicochemical structure of these hybrid membranes can be characterized and then used to design for a desired performance.

1. Introduction

Purification *via* separations is integral to modern chemical production, ranging from refining petroleum to manufacturing pharmaceuticals.[1,2] However, current industrial chemical separation processes are often energy intensive and estimated to be responsible for as much as 10–15% of global energy consumption.[3] Consequently, the development of more energy efficient and lower-cost separation processes is an active area of research.

Membrane-based separation processes are attractive due to their energy efficiency and ability to be electrified. Unlike thermally-driven methods that rely on energy-intensive phase changes or sorption processes, membranes operate through selective permeability. This approach enables highly efficient separations with lower energy consumption and reduced environmental impact compared with thermally-driven techniques. Membrane technology has found applications in areas such as reverse osmosis for water desalination,[4,5] gas separation for carbon capture,[6] and organic solvent reverse osmosis.[7] As the demand for sustainable and energy-efficient solutions continues to grow, the role of membranes in chemical separations is becoming increasingly important.

Polymers of intrinsic microporosity (PIMs) are a promising class of organic membranes for separations.[8–10] Owing to their rigid structure, PIMs tend to have a high degree of microporosity. PIM-1, a prototypical PIM, is a solution-processible microporous polymer membrane with a large free volume, making it an excellent choice for many separations.[8,11–13] However, as with many organic materials, PIMs are susceptible to dissolution or swelling in organic solvents, preventing their use in many organic solvent reverse osmosis (OSRO) separation processes.

Recently, vapor phase infiltration (VPI) has emerged as a novel approach to stabilize polymeric materials for organic separations.[14] VPI is a vapor deposition technique that generates hybrid organic–inorganic materials with material properties unique from the

[a] *School of Materials Science and Engineering, Atlanta, USA. E-mail: losego@gatech.edu*
[b] *School of Chemical and Biomolecular Engineering, Georgia Institute of Technology, Atlanta, GA, 30332, USA*

† Electronic supplementary information (ESI) available. See DOI: https://doi.org/10.1039/d4cp04645e

parent polymer. During VPI a polymeric material is exposed to a vapor-phase metal–organic precursor that sorbs into, diffuses throughout, and then becomes entrapped within the polymer matrix. Co-reacting the entrapped metal organic species with water vapor generates air-stable metal oxyhydroxide species distributed throughout the polymer matrix. This technique has been used to generate hybrid materials for a wide range of applications.[15–17] Importantly, VPI has been used to generate hybrid PIM-1/MO_xH_y membranes that are solvent stable without significant modifications to the polymeric material itself. These hybrid membranes represent an entirely new approach to achieving advanced separations from initially polymeric membranes.[18] While initial demonstration of VPI hybrid membranes have been promising, many fundamental questions remain to fully design and optimize these complex materials.

The interactions between polymer and metal–organic precursors in a VPI process are complicated and can vary with different polymer/precursor chemistries as well as with processing conditions.[19–23] Because VPI infiltrates small inorganic clusters that lack any long range ordering, exact characterization of the resulting inorganic chemical structure is challenging. Several advanced characterization techniques have been reported to try to better characterize these hybrid structures. TEM has been used to probe the atomic clusters selectively infiltrated in block co-polymers.[24,25] Pair distribution function (PDF) analysis of X-ray spectroscopy has been used to probe the structure of smaller amorphous clusters.[26] Recently, our group has used ^{27}Al NMR to study the local structure of Al in PIM-1/AlO_xH_y hybrid membranes.[21] Here, we found that upon one-cycle of infiltration, aluminum likely forms clusters that are at least dimerized and that these clusters likely have water ligands coordinated to the aluminum to achieve 6-fold (octahedrally-coordinated) aluminum species. We further showed that these inorganic structures vary as a function of processing parameters such as the use of post-infiltration dehydration and hydration steps.[27] In this work, we use a series of spectroscopy techniques including advanced X-ray absorption spectroscopies to explore the structure of infiltrated ZnO_xH_y in PIM-1 hybrid membranes, how the structure varies as a function of inorganic loading and number of cycles, and the role these structural changes have on the membrane's solvent stability.

2. Experimental methods

2.1. Vapor phase infiltration

Vapor phase infiltration was applied to polymer of instrinsic microporosity 1 (PIM-1), a common membrane material of interest for chemical separations.[28] Vapor phase infiltration was conducted in an isothermally controlled, hot wall reactor as previously described.[21,29] PIM-1 was initially soaked in methanol and subsequently dried in a fume hood to restore the polymer's structure prior to infiltration. The polymer was then placed in a reactor maintained at 90 °C and purged with ultrahigh purity (UHP) nitrogen (Airgas, 99.999%) for 5 hours to eliminate residual water and methanol. After purging, the chamber was evacuated to a rough vacuum of approximately 30 mTorr and then isolated. Diethyl zinc (DEZ, Strem Chemicals, DANGER: pyrophoric) was introduced from a room temperature precursor bottle, reaching a controlled partial pressure between 0.3 and 0.7 Torr. For our 28 L system equipped with valves rated with a flow coefficient (C_v) of 0.27, this pressure range corresponds to opening the DEZ valve for 1 to 3 seconds. The precursor was allowed to remain in contact with the sample for 1 to 24 hours before the chamber was again pumped to 30 mTorr for 1 hour to remove excess DEZ. Following this, a water vapor dose of 1.8 Torr was introduced, and the sample was held under these conditions for 5 hours. This represents a single VPI cycle. After one or more VPI cycles, samples were subjected to a final nitrogen purge prior to bringing the chamber to atmosphere. Reaction with water vapor results in the formation of an air-stable hybrid material, where $ZnO_x(OH)_y$ species are distributed within the polymer's free volume. Chamber pressure was monitored using a Baratron capacitance manometer. Both PIM-1 powders (for XAS characterization) as well as hollow fibers were infiltrated. PIM-1 powders were used for X-ray absorption spectroscopy (XAS). For all other characterization measurements, PIM-1 hollow fibers were used. However, no differences were observed in either form factor. Unless otherwise noted, all materials were infiltrated at 90 °C at a precursor pressure of 0.3 Torr for varying exposure times ranging from 1 h to 24 h.

2.2. Quantifying inorganic loading

Inorganic loadings were determined by thermogravimetric analysis of the hybrid membranes using a PerkinElmer TGA 4000. For all materials, 5 to 15 mg PIM-1/ZnO_xH_y was placed in the TGA and heated to 120 °C under air and held at 120 °C for 90 minutes to remove any sorbed water. Hybrids were then heated to 800 °C at 10 °C min^{-1}. Hybrid membranes were fully decomposed by 800 °C under ambient conditions (Fig. S1, ESI†). After reaching 800 °C, the sample was then and cooled at 10 °C min^{-1} back to 120 °C and held at 120 °C for 20 minutes. The initial and final mass was taken as the mass after each hold at 120 °C. The final mass divided by the initial mass was taken as the weight percent inorganic loading.

2.3. Atomic structure

XPS was performed using a Thermo Scientific K-Alpha XPS system using a monochromatic Al Kα X-ray source (1486.6 eV). Prior to measurement samples were pumped down under vacuum for 1 h. The pressure reached during analysis was $\sim 10^{-8}$ mbar. A pass energy of 50 eV was used. During measurement, scans were taken with a 0.100 eV step size. All XPS fittings were done using the Thermo Scientific Avantage software.

EXAFS measurements were taken on a lab scale easyXAFS 300+ previously described by Krishanan *et al.*[30] XAS data were normalized using the Athena software package before the analysis of K-edge positions.[31] The edge position was determined by using the maximum of the first derivative of the absorption spectrum. Simulated EXAFS spectra were generated

using the Artemis software package. Zinc structures were generated and imported into the Artemis software package, which calculated each scattering pattern. Each single and multiple scattering pattern generated in Artemis was included in the simulated FT-EXAFS spectrum.

2.4. Dissolution testing

To determine the rates of membrane dissolution, hybrid samples were placed in 20 ml of THF, a good solvent for the pure PIM-1 polymer. UV-Vis spectra were taken at regular time intervals using an Avantes StarLine AvaSpec 2048 detector with a built-in halogen light source. Prior to measurements, the light source was allowed to warm up for 15 min. Light and dark references were taken of THF prior to placing PIM-1 fibers in the THF. Calibration curves were used to convert peak absorbance to mass dissolved according to Beers law. The peak absorbance for the peak at 370 nm was tracked and converted to mass dissolved for each UV-Vis spectra.

3. Results & discussion

3.1. Effects of inorganic loading on the chemical stability of PIM-1/ZnO_xH_y hybrid membranes

We previously demonstrated that in undersaturated conditions, exposure time and precursor dose pressure can be used to modify and control the inorganic loading.[32,33] Varying the infiltrated inorganic loading can be used to modify various properties in the hybrid material. For example, infiltrating PIM-1 hybrid membranes with varying amounts of inorganic can alter the solvent stability and separation performance.[18] For other hybrid systems, we have shown that systematic variations in inorganic loading lead to systematic changes in the glass transition temperature of the hybrid material.[34]

Here, we use variations in diethyl zinc (DEZ) exposure time and pressure to alter the amount of ZnO_xH_y loading into these hybrid PIM-1/ZnO_xH_y membranes. Fig. 1 plots the solvent stability for hybrid PIM-1/ZnO_xH_y membranes infiltrated at 90 °C at varying exposure times and DEZ partial pressures using just 1 cycle of exposure. We then sort each of these membranes based on their weight percent of inorganic loading as measured with TGA. Prior reports have demonstrated that untreated PIM-1 membranes fully dissolve in 100 min.[35] While hybrid membranes loaded with only 4 wt% ZnO_xH_y begin to rapidly dissolve after 10 min of immersion in THF with fully half the membrane dissolved within 30 min, hybrid membranes loaded to 10 wt% ZnO_xH_y are not half dissolved until after 20 days of immersion. These results underscore the possibility of using VPI process conditions to control the inorganic structure in these hybrid materials and tailor resultant properties. In the remaining sections of this paper, we seek to better understand the physicochemical structure of these hybrids and reveal that dissolution resistance may involve more than just the amount of inorganic content in the material but also the chemical structure of that inorganic (hydroxide *versus* oxide) and the size of the inorganic networks.

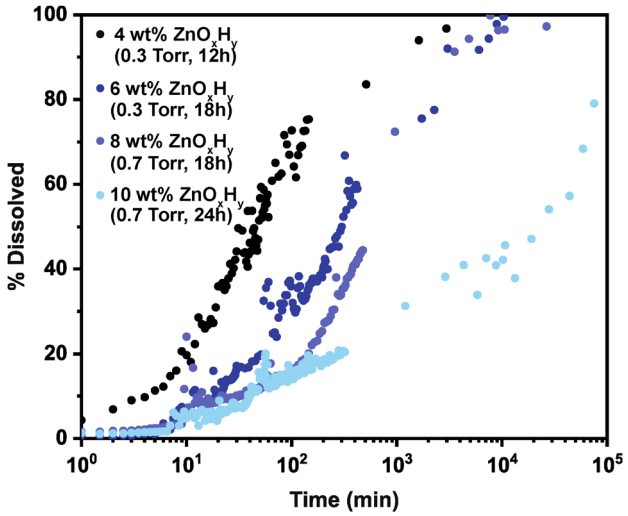

Fig. 1 Percent of the hybrid PIM-1/ZnO_xH_y membrane that dissolves as a function of time (logscale) upon immersion in THF at room temperature. Varying inorganic loading fractions from 4 wt% to 10 wt% ZnO_xH_y in the hybrid membranes are achieved based on precursor exposure times and overpressures.

3.2. Spectroscopic investigation of inorganic cluster chemistry and growth upon 1 cycle of infiltration

Fig. 2 presents representative XPS results for the PIM-1/ZnO_xH_y hybrid structure at 10 wt% inorganic loading. Similar to other hybrid PIM-1 systems, the N 1s (399.4 eV) and C 1s (286.7 eV, 284.5 eV) XPS spectra (Fig. 2a and b) show no significant deviations from the pure polymer, suggesting that no chemical linkages form to the polymer's C, N, or O species.[21] Instead, infiltrated Zn appears to remain as an unbound inorganic in a 2+ oxidation state (1022 eV) (Fig. 2d),[35] which according to the O 1s spectrum (Fig. 2c) is in a highly hydrated form consisting

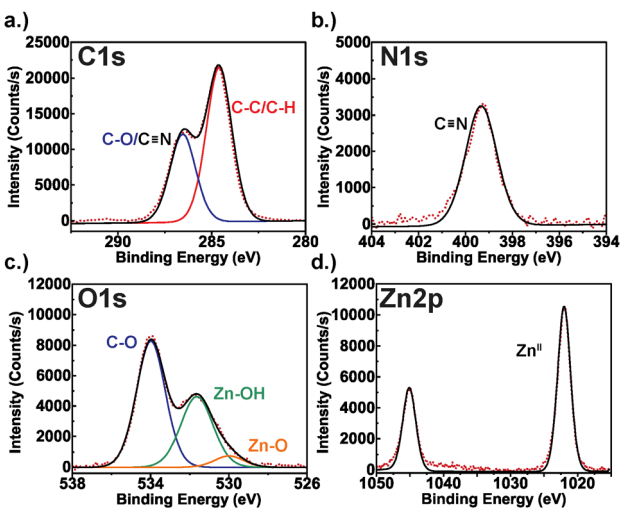

Fig. 2 Core level XPS spectra of PIM-1/ZnO_xH_y (10 wt%) after 1 cycle of infiltration at 90 °C, 24 h exposure, and 0.7 Torr dose pressure: (a) C 1s, (b) N 1s, (c) O 1s, and (d) Zn 2p. Here, red dots represent experimental data, while the fitted result is shown in black.

of 87% $Zn(OH)_2$ (531.6 eV) and 13% ZnO (529.7 eV) by relative peak area composition.[36]

Fig. 3 presents XPS data that further interrogates the extent of ZnO_xH_y hydration at the various inorganic loading conditions originally presented in Fig. 1. Here we show deconvoluted O 1s spectra for each of these PIM-1/ZnO_xH_y membranes. For all conditions, the inorganic appears to be predominantly a hydroxide with minimal (13–25%) oxide character. As expected, the intensity of Zn–OH and Zn–O absorptions increase relative to the C–O peak of the polymer with increasing inorganic loading. However, the variation in hydroxide-to-oxide fraction is modest for these different loading fractions and likely just a result of experimental variations. Thus, extended exposure times or variations in precursor overpressure do not appear to substantially alter the chemical structure (*i.e.*, extent of hydration) of the inorganic.

To gain more information about the inorganic cluster structure and size, more advanced spectroscopic tools are needed. For example, EXAFS spectroscopy is sensitive to the coordination environment beyond just the nearest-neighbor detected in XPS. Here, we explore the use of Zn K-edge EXAFS to gain additional information about changes in the inorganic coordination spheres and cluster size. Fig. 4(a) plots the Fourier-transformed Zn K-edge EXAFS spectra for PIM-1/ZnO_xH_y at the various inorganic loading fractions initially presented in Fig. 1. Two major peaks are apparent in the EXAFS spectra at $\approx$1.6 Å and $\approx$2.8 Å. EXAFS measurements of pure ZnO and $Zn(OH)_2$ suggest that the first peak is associated with the Zn–O single scattering interaction (1.6 Å), while the second peak can be attributed to Zn–Zn correlations as well as Zn–O multiple scattering (MS) interactions that typically manifest as a broad combined peak between 2.4 Å and 3.6 Å.[37,38] These values correspond well with the EXAFS reported here for infiltrated

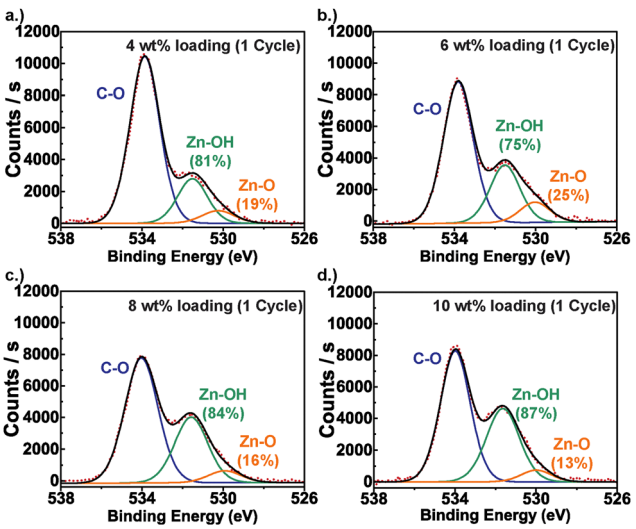

Fig. 3 XPS O 1s spectra of PIM-1/ZnO_xH_y hybrid membranes of increasing inorganic loadings infiltrated at 90 °C: (a) 4 wt% inorganic loading, (b) 6 wt% inorganic loading, (c) 8 wt% inorganic loading, and (d) 10 wt% inorganic loading. Here, red dots represent experimental data, while the fitted result is shown in black.

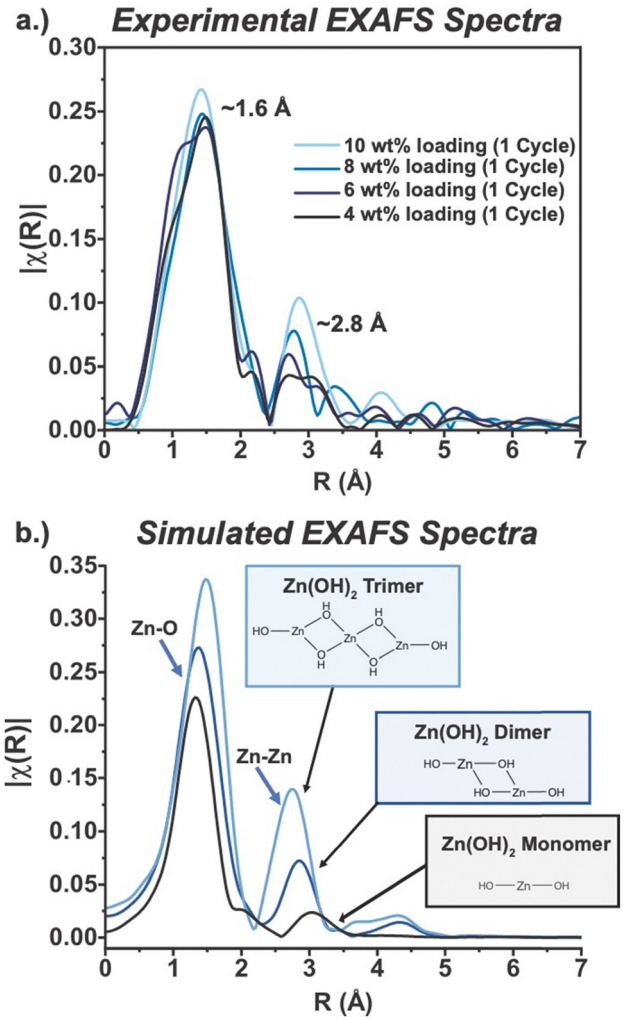

Fig. 4 (a) Experimental EXAFS spectra for increasing inorganic loadings; (b) simulated EXAFS spectra for Zn–OH clusters of increasing size.

PIM-1/ZnO_xH_y. While this Zn–O peak at 1.6 Å changes modestly with inorganic loading, we attribute these minor differences to be primarily from mean square relative distance (MSRD) rather than coordination number. Significant differences are observed in the Zn–Zn scattering peak at $\sim$2.8 Å. Specifically, this peak systematically increases in both size and intensity with increasing inorganic loadings. While this peak appears at a much lower intensity, the good signal to noise ratio ensures that conclusions about this peak can be made with reasonable confidence.

First, it is noteworthy that even just the presence of a Zn–Zn scattering interaction suggests that clusters of at least two Zn atoms are forming. Specifically, this excitation is evidence that Zn atoms exist in a second coordination shell of a central zinc atom, and that these zinc's have about the same distance amongst all clusters. The observed increase in this peak's intensity with inorganic loading can likely be attributed to an increases in the coordination number in this coordination shell, or in other words, more next nearest neighbor Zn atoms.[39] In the context of infiltrated ZnO_xH_y, we postulate that

this increase in EXAFS intensity indicates an increase in the inorganic cluster size. The high hydroxide content detected in XPS further suggests that these clusters are likely growing through a mineralization process *via* bridging hydroxide bonds. This would indicate that increasing exposure times leads to the formation of larger $[Zn(OH)_2]_x$ clusters, and that the improvement in solvent stability is largely due to the formation of these larger clusters at increased exposure times.

To provide further evidence for this cluster size argument, Fig. 4(b) shows the simulated EXAFS spectra for various cluster sizes. Because the XPS suggests a primarily hydroxide character, these simulations are run only for $[Zn(OH)_2]_x$ clusters, specifically for the monomer, dimer, and trimer. Here, the central Zn atom within the trimer represents a $[ZnO_4]$ type cluster. We note that the structures are optimized to be in their lowest energy state. These structures were simulated by including all single and multiple scattering interactions generated from FEFF calculations in Athena; no EXAFS fitting to the experimental EXAFS spectra was done. As shown, the simulated EXAFS spectra resemble the experimentally measures EXAFS spectra with major peaks at 1.6 Å and 2.8 Å. Minor differences in the spectra could be due to the presence of the other scattering interactions from the organic polymer. Increasing cluster size from the Zn monomer (in leads to increases in the Zn–Zn peak, similar to what is observed experimentally).

Previous studies of $Zn(OH)_2$ have shown that the 2.8 Å scattering event can be a combination of Zn–Zn single scattering interactions and Zn–O multiple scattering events.[37] The correlation between EXAFS scattering amplitude's, $F(k)$, and an element's atomic number (Z) can be used to differentiate amongst these scattering events. By removing the low-k region of the EXAFS spectrum and then applying the Fourier transform it is possibly to highlight scattering events caused primarily by higher atomic number species.[37] The effects of removing the low k region of the FT-EXAFS (k values of < 3.5 Å) is presented in Fig. 5. Here, the spectra including the low-k values are plotted in solid black lines while the spectra excluding these low-k values are plotted in dotted red lines. In general, the removal of the low-k scattering is expected to reduce scattering from oxygen (*e.g.*, Zn–O multiscattering) but retain scattering from Zn (*e.g.*, Zn–Zn single scattering). As shown, the first shell (Zn–O single scattering) is very sensitive to the low k region and decreases significantly when this region is excluded, consistent with the significant scattering from oxygen needed for this Zn–O single scattering inetraction. More interesting is the observed changes in the second shell. For 4 and 6 wt% loading (Fig. 5a and b), the second shell peak is significantly reduced upon removing the low-k scattering, suggesting much of this scattering is from Zn–O multiscattering events. This result suggests that Zn–Zn scattering is not a significant contributor at these concentrations and thus clusters may not yet be forming (majority monomers). At higher inorganic loadings of 8 and 10 wt% (Fig. 5c and d), this second shell scattering event loses some intensity but still retains a clear scattering signal, suggesting that Zn–Zn single scattering is a significant contributor. Additionally, analysis of scattering paths of

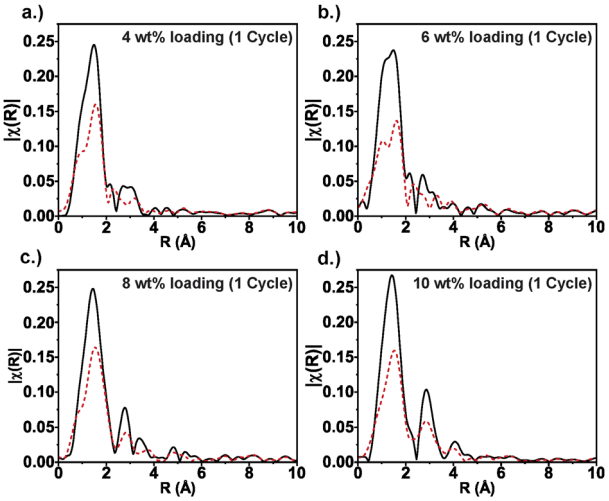

Fig. 5 EXAFS spectra for (a) 4 wt%; (b) 6 wt%; (c) 8 wt%; and (d) 10 wt% PIM-1/ZnO_xH_y at varying k-ranges. Δk =1.5–9.5 Å^{-1} (solid Line), Δk 3.5–9.5 Å^{-1} (dotted line).

simulated structures shown in Table S4 (ESI†) indicates that the Zn–Zn single scattering path is a much stronger path than the Zn–O multiple scattering paths. This result portends that the clusters are growing larger (dimer to trimer size) upon reaching higher inorganic loading fractions.

In summary, the change in inorganic loading from just a single-cycle of ZnO_xH_y VPI appears to not change the chemical nature of the infiltrated inorganic (it is primarily hydroxide), but does alter the size of the clusters. Both the increase in intensity of the Zn–Zn scattering peak and its increased origin from Zn–Zn single scattering events provides the evidence that these inorganic clusters are increasing in size, and these structural changes are presumably contributing to the increased resistance to chemical dissolution observed in Fig. 1.

3.3. Effects of increased infiltration cycles

Conceivably, other process parameters may influence inorganic cluster growth in these hybrid materials. One important parameter that has routinely had an important influence on observed properties is the number of VPI cycles. However, it is unclear if the number of cycles is simply increasing the inorganic loading or if cycling also affects the inorganic structure. Here we attempt to address this question by running 1, 2, and 3 VPI cycles on PIM-1 using 12, 5, and 1 h DEZ exposure times to achieve equivalent inorganic loadings ($\sim$4 wt%) at varying cycle numbers. Fig. 6 plots the solvent stability for these three materials. Interestingly, even though these hybrid membranes have equivalent inorganic loadings, they exhibit varying dissolution rates, suggesting that each hybrid has differences in their physicochemical structures. These hybrid membranes specifically demonstrate an increased solvent stability with more VPI cycle numbers despite having relatively equivalent inorganic fractions.

To understand difference in atomic structure, various spectroscopies are conducted on these materials. Fig. 7a plots the

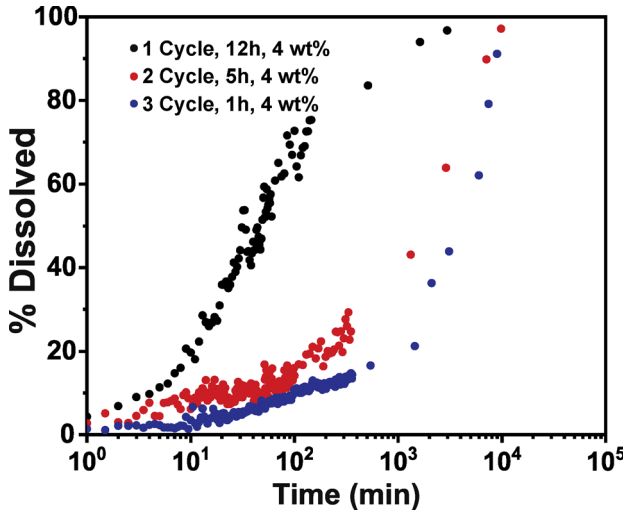

Fig. 6 Dissolution of PIM-1/ZnO_xH_y membranes infiltrated at 90 °C for 1 cycle (0.3 Torr, 12 h exposure), 2 cycles (0.3 Torr, 5 h exposure), and 3 cycles (0.3 Torr, 1 h exposure).

hydroxide and oxide fractions of the infiltrated ZnO_xH_y clusters in these hybrid membranes as determined from the XPS O 1s spectra. Here, the fraction of oxide increases with the number of VPI cycles going from 19% oxide at 1 cycle to 50% oxide at 3 cycles. This result suggests that a change in chemical character from hydroxide to oxide is occurring with cycle number and this change in chemical character may be contributing to the increased chemical stability observed in Fig. 6.

Fig. 7b shows the Zn k-edge EXAFS spectra for these three hybrid membranes. Interestingly, 1 and 2 cycles of infiltration show similar EXAFS spectra, even though the solvent stability is much improved from one to two cycles. In contrast, significant changes in the EXAFS pattern are observed from 2 to 3 VPI cycles. First, a notable increase in the Zn–Zn peak is observed. However, because the total inorganic loading remains constant—meaning this intensity increase is not simply due to a higher concentration of inorganic content—the enhanced Zn–Zn peak suggests the presence of more Zn in the second coordination shell, implying the formation of larger clusters at higher cycle counts. Additionally, the shoulder on the Zn–O EXAFS peak becomes less pronounced with increasing cycles. This could be due to the evolution from $Zn(OH)_2$ to ZnO or from the coordination of water ligands in small Zn hydroxide clusters which have slightly longer bond lengths than Zn–O and Zn–OH. Smith *et al.* proposed that water ligands coordinate to zinc hydroxide molecular clusters to stabilize the complex during cluster growth.[40] The shoulder observed in smaller clusters could result from these water ligands, explaining why it is less pronounced with increasing cluster size. Additional comparison data and reference spectra are included in Fig. S9 and S10 (ESI†).[41,42]

As the oxide content increases with additional VPI cycles, as indicated by XPS, it suggests that not only does increased clustering contribute to solvent stability, but the structural composition (ZnO *vs.* $Zn(OH)_2$) also plays a crucial role. Fig. 7c attempts to capture the chemical and structural changes that stabilize the hybrid membrane. As indicated, during 1 cycle of infiltration, more, but smaller, clusters form throughout the polymer matrix. During 2 cycles, the exposure time is shortened to maintain the same inorganic loading. This results in fewer but larger clusters compared to one cycle. This trend continues further with 3 cycles, leading to the formation of the fewest but largest clusters within the PIM-1 membrane.

Finally, we compare processing conditions where the number of VPI cycles is held constant (2 cycles total) but the precursor pressure is varied to alter the total amount of

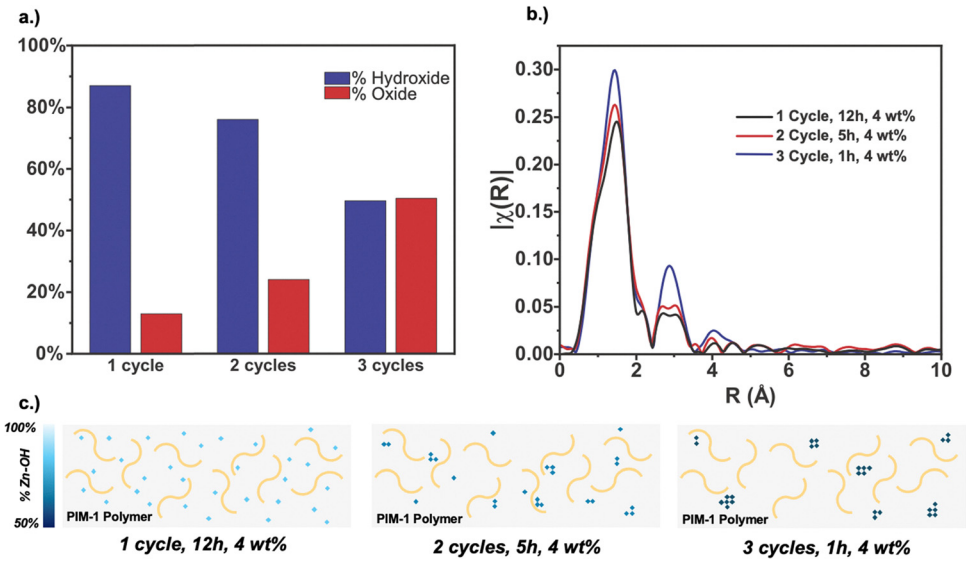

Fig. 7 (a) % hydroxide and % oxide as a function of cycle count in PIM-1/ZnO_xH_y; (b) Zn K-edge EXAFS spectra for PIM-1/ZnO_xH_y infiltrated for 1, 2, and 3 cycles at 0.3 Torr, resulting in 4% inorganic loading; (c) depiction of hybrid membrane structure at each VPI condition. Here, blue diamonds represent infiltrated ZnO_xH_y clusters and yellow lines represent PIM-1.

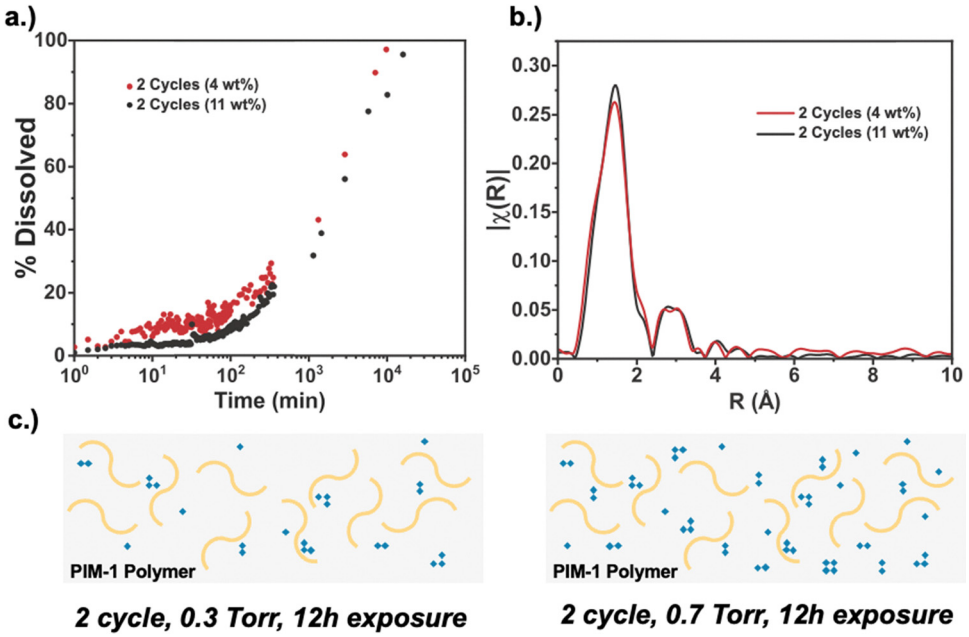

Fig. 8 (a) Dissolution in THF of PIM-1/ZnO_xH_y membranes infiltrated at 90 °C for 2 cycles; (b) corresponding EXAFS spectra; (c) depiction of hybrid membrane structure at each VPI condition. Blue diamonds represent infiltrated ZnO_xH_y clusters.

inorganic loading. Specifically, we compare hybrid membranes formed from 2 VPI cycles having 12 h of DEZ exposure at 0.3 and 0.7 Torr, resulting in 4 and 11 wt% inorganic loading, respectively. Here, the 4 wt% condition is similar to the 2-cycle material presented in Fig. 7. *Via* XPS (S2), both hybrids are measured to have similar oxide character, with the 4 wt% inorganic loaded material containing 27% oxide character and the 11 wt% inorganic loaded material containing 35% oxide character. Fig. 8a plots the solvent stability for these hybrid membranes. As expected, the higher inorganic loading membrane has better solvent stability, although not dramatically higher. On average, the 11 wt% loaded membranes exhibits ~5–10% less dissolution at each time point compared to the 4 wt% loaded membrane. Interestingly, the EXAFS spectra in Fig. 8b are similar for these two materials despite having very different inorganic loadings. The similar intensity of the Zn–Zn peak indicates that the clusters in both samples are similar in size, and thus, cluster size is not varying between the two. The ability to achieve a different EXAFS structure, as was observed for 3 cycles in Fig. 7b, appears to require more cycles and cannot just be achieved with more exposure time, despite the higher inorganic loading. Fig. 8(c) illustrates a postulated structure for these two hybrid materials. Here, both membranes have the same cluster sizes and hydration states, with the higher loaded material simply having more of these clusters. We speculate that this is why the higher loading sample has better solvent stability. However, the moderate increase in solvent stability indicates that the primary driver of solvent stability may be due to increases in the size of the inorganic clusters, and possibly the chemical transition from hydroxide to oxide, more so than just the number of infiltrated inorganic clusters.

4. Conclusion

In this work, spectroscopic analysis has been conducted to deduce the physical and chemical features contributing to the chemical stability of hybrid PIM-1/ZnO_xH_y membranes. These measurements provide new insights into how ZnO_xH_y inorganics grow within a polymer matrix. These structural features are then compared back to the solvent stability performance of the hybrid material. EXAFS analysis was used to understand coordination in the first and second shells beyond Zn. Increasing the exposure time of the metal–organic vapor provided evidence for the growth of zinc hydroxide clusters to sizes that included more than one zinc atom. However, the character of these inorganic clusters remained largely (~80%) hydroxide. Increasing the number of infiltration cycles appears to influence both the cluster size and the chemical character of the inorganic clusters. At three vapor phase infiltration cycles, the inorganic clusters become 50% hydroxide and 50% oxide in character. Both the growth in the inorganic cluster size and the change in character from hydroxide to oxide appears to improve the solvent stability of the final hybrid material. Interestingly, several of the systems explored here seem to show minimal changes in solvent stability with just increases in overall inorganic loading fraction of the material. Thus, these results suggest that the actual structure of the inorganic (*e.g.*, cluster size and chemical characteristics) may have a greater influence on stabilizing the hybrid against dissolution than just simply increasing the concentration of inorganic in the material.

Conflicts of interest

There are no conflicts to declare.

Data availability

The data supporting this article have been included as part of the ESI.†

Acknowledgements

This work was financially support by the National Science Foundation through DMREF-1921873 and MRI-1925797, which supported the acquisition of the easyXAFS X-ray absorption spectrometer used in this study. A portion of this work was also performed at the Georgia Tech Institute for Matter and Systems, a member of the National Nanotechnology Coordinated Infrastructure (NNCI), which is supported by the National Science Foundation (ECCS-2025462). Any opinions, findings, and conclusions or recommendations expressed in this material are those of the authors and do not necessarily reflect the views of the National Science Foundation.

References

1 H. Strathmann, Membrane separation processes: Current relevance and future opportunities, *AIChE J.*, 2001, **47**(5), 1077–1087, DOI: **10.1002/aic.690470514**.

2 B. Liang, X. He, J. Hou, L. Li and Z. Tang, Membrane Separation in Organic Liquid: Technologies, Achievements, and Opportunities, *Adv. Mater.*, 2019, **31**(45), 1806090, DOI: **10.1002/adma.201806090**.

3 D. S. Sholl and R. P. Lively, Seven chemical separations to change the world, *Nature*, 2016, **532**(7600), 435–437, DOI: **10.1038/532435a**.

4 D. Cohen-Tanugi, R. K. McGovern, S. H. Dave, J. H. Lienhard and J. C. Grossman, Quantifying the potential of ultra-permeable membranes for water desalination, *Energy Environ. Sci.*, 2014, **7**(3), 1134–1141, DOI: **10.1039/C3EE43221A**.

5 M. Drobek, C. Yacou, J. Motuzas, A. Julbe, L. Ding and J. C. Diniz da Costa, Long term pervaporation desalination of tubular MFI zeolite membranes, *J. Membr. Sci.*, 2012, **415–416**, 816–823, DOI: **10.1016/j.memsci.2012.05.074**.

6 C. Shah, S. Raut, H. Kacha, H. Patel and M. Shah, Carbon capture using membrane-based materials and its utilization pathways, *Chem. Pap.*, 2021, **75**(9), 4413–4429, DOI: **10.1007/s11696-021-01674-z**.

7 W. J. Koros and C. Zhang, Materials for next-generation molecularly selective synthetic membranes, *Nat. Mater.*, 2017, **16**(3), 289–297, DOI: **10.1038/nmat4805**.

8 I. I. Ponomarev, D. Y. Razorenov, I. V. Blagodatskikh, A. V. Muranov, L. E. Starannikova, A. Y. Alent'ev, R. Y. Nikiforov and Y. P. Yampol'skii, Polymer with Intrinsic Microporosity PIM-1: New Methods of Synthesis and Gas Transport Properties, *Polym. Sci., Ser. B*, 2019, **61**(5), 605–612, DOI: **10.1134/S1560090419050142**.

9 J. Gao, S. Japip and T.-S. Chung, Organic solvent resistant membranes made from a cross-linked functionalized polymer with intrinsic microporosity (PIM) containing thioamide groups, *Chem. Eng. J.*, 2018, **353**, 689–698, DOI: **10.1016/j.cej.2018.07.156**.

10 Y. Shin, E. Prestat, K.-G. Zhou, P. Gorgojo, K. Althumayri, W. Harrison, P. M. Budd, S. J. Haigh and C. Casiraghi, Synthesis and characterization of composite membranes made of graphene and polymers of intrinsic microporosity, *Carbon*, 2016, **102**, 357–366, DOI: **10.1016/j.carbon.2016.02.037**.

11 P. Číhal, M. Dendisová, M. Švecová, Z. Hrdlička, T.-M. Durďáková, P. M. Budd, W. Harrison, K. Friess and O. Vopička, Sorption, swelling and plasticization of PIM-1 in methanol-dimethyl carbonate vapour mixtures, *Polymer*, 2021, **218**, 123509, DOI: **10.1016/j.polymer.2021.123509**.

12 M. L. Jue, C. S. McKay, B. A. McCool, M. G. Finn and R. P. Lively, Effect of Nonsolvent Treatments on the Microstructure of PIM-1, *Macromolecules*, 2015, **48**(16), 5780–5790, DOI: **10.1021/acs.macromol.5b01507**.

13 P. M. Budd, N. B. McKeown, B. S. Ghanem, K. J. Msayib, D. Fritsch, L. Starannikova, N. Belov, O. Sanfirova, Y. Yampolskii and V. Shantarovich, Gas permeation parameters and other physicochemical properties of a polymer of intrinsic microporosity: Polybenzodioxane PIM-1, *J. Membr. Sci.*, 2008, **325**(2), 851–860, DOI: **10.1016/j.memsci.2008.09.010**.

14 E. K. McGuinness, C. Z. Leng and M. D. Losego, Increased Chemical Stability of Vapor-Phase Infiltrated AlOx–Poly(methyl methacrylate) Hybrid Materials, *ACS Appl. Polym. Mater.*, 2020, **2**(3), 1335–1344, DOI: **10.1021/acsapm.9b01207**.

15 I. Azpitarte, G. A. Botta, C. Tollan and M. Knez, SCIP: a new simultaneous vapor phase coating and infiltration process for tougher and UV-resistant polymer fibers, *RSC Adv.*, 2020, **10**(27), 15976–15982, DOI: **10.1039/D0RA02073G**.

16 C. Z. Leng and M. D. Losego, Vapor phase infiltration (VPI) for transforming polymers into organic–inorganic hybrid materials: a critical review of current progress and future challenges, *Mater. Horiz.*, 2017, **4**(5), 747–771, DOI: **10.1039/C7MH00196G**.

17 W. Wang, F. Yang, C. Chen, L. Zhang, Y. Qin and M. Knez, Tuning the Conductivity of Polyaniline through Doping by Means of Single Precursor Vapor Phase Infiltration, *Adv. Mater. Interfaces*, 2017, **4**(4), 1600806, DOI: **10.1002/admi.201600806**.

18 Y. Ren, B. C. Jean, W. J. Jang, A. Sarswat, Y. J. Lee, E. K. McGuinness, K. Dhavala, M. D. Losego and R. P. Lively, Engineering organic solvent reverse osmosis in hybrid AlO_xH_y/polymer of intrinsic microporosity 1 (PIM-1) membranes using vapor phase infiltration, *J. Memb. Sci. Lett.*, 2023, **3**(2), 100064, DOI: **10.1016/j.memlet.2023.100064**.

19 C. Z. Leng and M. D. Losego, A physiochemical processing kinetics model for the vapor phase infiltration of polymers: measuring the energetics of precursor-polymer sorption, diffusion, and reaction, *Phys. Chem. Chem. Phys.*, 2018, **20**(33), 21506–21514, DOI: **10.1039/C8CP04135K**.

20 E. C. Dandley, C. D. Needham, P. S. Williams, A. H. Brozena, C. J. Oldham and G. N. Parsons, Temperature-dependent reaction between trimethylaluminum and poly(methyl methacrylate) during sequential vapor infiltration: experimental and ab initio analysis, *J. Mater. Chem. C*, 2014, **2**(44), 9416–9424, DOI: **10.1039/C4TC01293C**.

21 Y. Liu, E. K. McGuinness, B. C. Jean, Y. Li, Y. Ren, B. G. Rio, R. P. Lively, M. D. Losego and R. Ramprasad, Vapor Phase Infiltration of Polymer of Intrinsic Microporosity 1 (PIM-1) with Trimethylaluminum (TMA) and Water: A combined computational and experimental study, *Chem. Mater.*, 2022, **126**(31), 5920–5930, DOI: **10.1021/acs.jpcb.2c01928**.

22 I. Azpitarte, A. Zuzuarregui, H. Ablat, L. Ruiz-Rubio, A. López-Ortega, S. D. Elliott and M. Knez, Suppressing the Thermal and Ultraviolet Sensitivity of Kevlar by Infiltration and Hybridization with ZnO, *Chem. Mater.*, 2017, **29**(23), 10068–10074, DOI: **10.1021/acs.chemmater.7b03747**.

23 S. Obuchovsky, I. Deckman, M. Moshonov, T. Segal Peretz, G. Ankonina, T. J. Savenije and G. L. Frey, Atomic layer deposition of zinc oxide onto and into P3HT for hybrid photovoltaics, *J. Mater. Chem. C*, 2014, **2**(42), 8903–8910, DOI: **10.1039/C4TC01629G**.

24 T. Segal-Peretz, J. Winterstein, M. Doxastakis, A. Ramírez-Hernández, M. Biswas, J. Ren, H. S. Suh, S. B. Darling, J. A. Liddle and J. W. Elam, *et al.*, Characterizing the Three-Dimensional Structure of Block Copolymers *via* Sequential Infiltration Synthesis and Scanning Transmission Electron Tomography, *ACS Nano*, 2015, **9**(5), 5333–5347, DOI: **10.1021/acsnano.5b01013**.

25 O. M. Ishchenko, S. Krishnamoorthy, N. Valle, J. Guillot, P. Turek, I. Fechete and D. Lenoble, Investigating Sequential Vapor Infiltration Synthesis on Block-Copolymer-Templated Titania Nanoarrays, *J. Phys. Chem. C*, 2016, **120**(13), 7067–7076, DOI: **10.1021/acs.jpcc.5b10415**.

26 X. He, R. Z. Waldman, D. J. Mandia, N. Jeon, N. J. Zaluzec, O. J. Borkiewicz, U. Ruett, S. B. Darling, A. B. F. Martinson and D. M. Tiede, Resolving the Atomic Structure of Sequential Infiltration Synthesis Derived Inorganic Clusters, *ACS Nano*, 2020, **14**(11), 14846–14860, DOI: **10.1021/acsnano.0c03848**.

27 B. C. Jean, Y. Ren, I. Slagle, R. P. Lively, F. M. Alamgir and M. D. Losego, *Chem. Mater.*, 2025, **37**(11), 3959–3968.

28 P. M. Budd, K. J. Msayib, C. E. Tattershall, B. S. Ghanem, K. J. Reynolds, N. B. McKeown and D. Fritsch, Gas separation membranes from polymers of intrinsic microporosity, *J. Membr. Sci.*, 2005, **251**(1), 263–269, DOI: **10.1016/j.memsci.2005.01.009**.

29 B. D. Piercy and M. D. Losego, Tree-based control software for multilevel sequencing in thin film deposition applications, *J. Vac. Sci. Technol., B*, 2015, **33**(4), 043201, DOI: **10.1116/1.4926676**.

30 A. Krishnan, D.-C. Lee, I. Slagle, S. Ahsan, S. Mitra, E. Read and F. M. Alamgir, Monitoring Redox Processes in Lithium-Ion Batteries by Laboratory-Scale Operando X-ray Emission Spectroscopy, *ACS Appl. Mater. Interfaces*, 2024, **16**(13), 16096–16105, DOI: **10.1021/acsami.3c18424**.

31 B. Ravel and M. Newville, ATHENA, ARTEMIS, HEPHAESTUS: data analysis for X-ray absorption spectroscopy using IFEFFIT, *J. Synchrotron Radiat.*, 2005, **12**(4), 537–541.

32 B. C. Jean, Y. Ren, E. K. McGuinness, R. P. Lively and M. D. Losego, Effects of trimethylaluminum vapor pressure and exposure time on inorganic loading in vapor phase infiltrated PIM-1 polymer membranes, *Mater. Chem. Phys.*, 2022, **290**, 126577, DOI: **10.1016/j.matchemphys.2022.126577**.

33 Y. Ren, E. K. McGuinness, C. Huang, V. R. Joseph, R. P. Lively and M. D. Losego, Reaction–Diffusion Transport Model to Predict Precursor Uptake and Spatial Distribution in Vapor-Phase Infiltration Processes, *Chem. Mater.*, 2021, **33**(13), 5210–5222, DOI: **10.1021/acs.chemmater.1c01283**.

34 J. T. Bamford, R. A. Smith, C. Z. Leng, W. R. Gutekunst and M. D. Losego, Measuring the Glass Transition Temperature of Vapor-Phase-Infiltrated AlOx-PS-r-PHEMA Organic–Inorganic Hybrid Thin-Film Materials, *Macromolecules*, 2021, **54**(14), 6790–6798, DOI: **10.1021/acs.macromol.1c00691**.

35 A. G. Marrani, F. Caprioli, A. Boccia, R. Zanoni and F. Decker, Electrochemically deposited ZnO films: an XPS study on the evolution of their surface hydroxide and defect composition upon thermal annealing, *J. Solid State Electrochem.*, 2014, **18**(2), 505–513, DOI: **10.1007/s10008-013-2281-2**.

36 N. J. Nicholas, G. V. Franks and W. A. Ducker, The mechanism for hydrothermal growth of zinc oxide, *CrystEngComm*, 2012, **14**(4), 1232–1240, DOI: **10.1039/C1CE06039B**.

37 K. I. Pandya, A. E. Russell, J. McBreen and W. O'Grady, EXAFS investigations of Zn (II) in concentrated aqueous hydroxide solutions. The, *J. Phys. Chem.*, 1995, **99**(31), 11967–11973.

38 J. Haug, A. Chassé, M. Dubiel, C. Eisenschmidt, M. Khalid and P. Esquinazi, Characterization of lattice defects by X-ray absorption spectroscopy at the Zn K-edge in ferromagnetic, pure ZnO films, *J. Appl. Phys.*, 2011, **110**(6), 063507, DOI: **10.1063/1.3631774**.

39 O. J. Dura, R. Boada, M. A. López de la Torre, G. Aquilanti, A. Rivera-Calzada, C. Leon and J. Chaboy, XANES and EXAFS study of the local order in nanocrystalline yttria-stabilized zirconia, *Phys. Rev. B*, 2013, **87**(17), 174109, DOI: **10.1103/PhysRevB.87.174109**.

40 G. D. Smith, R. Bell, O. Borodin and R. L. Jaffe, A Density Functional Theory Study of the Structure and Energetics of Zincate Complexes, *J. Phys. Chem. A*, 2001, **105**(26), 6506–6512, DOI: **10.1021/jp0100710**.

41 F. Yang, W. Hu, C. Yang, M. Patrick, A. L. Cooksy, J. Zhang, J. A. Aguiar, C. Fang, Y. Zhou and Y. S. Meng, Tuning internal strain in metal–organic frameworks *via* vapor phase infiltration for CO_2 reduction, *Angew. Chem.*, 2020, **132**(11), 4602–4610.

42 D. R. Roberts, R. G. Ford and D. L. Sparks, Kinetics and mechanisms of Zn complexation on metal oxides using EXAFS spectroscopy, *J. Colloid Interface Sci.*, 2003, **263**(2), 364–376.